1  # Quantifying Effects of Earth Orbital Parameters and
2  # Greenhouse Gases on Mid-Holocene Climate

3  Yibo Kang and Haijun Yang*

4  Department of Atmospheric and Oceanic Sciences and Institute of Atmospheric Science and CMA-FDU Joint

5  Laboratory of Marine Meteorology, Fudan University, Shanghai, 200438, China.

6  Shanghai Scientific Frontier Base for Ocean-Atmosphere Interaction Studies, Fudan University, Shanghai 200438,

7  China.

8  *Correspondence to*: Haijun Yang (yanghj@fudan.edu.cn)

9  **Abstract.** The mid-Holocene (MH) is the most recent typical climate period and a hot topic for global paleocultural

10  research. Following the latest Paleoclimate Modelling Intercomparison Project (PMIP) protocol and using a fully

11  coupled climate model, we simulated the climate difference between the MH and the pre-industrial (PI) periods, and

12  quantified the effects of Earth orbital parameters (ORB) and greenhouse gases (GHG) on climate difference. More

13  attention was paid to the simulated differences in the Atlantic meridional overturning circulation (AMOC) between

14  these two periods. Compared to the PI conditions, the ORB effect in the MH simulation led to the seasonal

15  enhancement of temperature, consistent with previous findings. For the MH simulation, the ORB effect led to a

16  remarkably warmer climate in the mid-high latitudes and increased precipitation in the Northern Hemisphere, which

17  were partially offset by the cooling effect of the lower GHG. The AMOC in the MH simulation was about 4% stronger

18  than that in the PI conditions. The ORB effect led to 6% enhancement of the AMOC in the MH simulation, which

19  was, however, partly neutralized by the GHG effect. The simulated stronger AMOC in the MH was mainly due to the

20  thinner sea ice in the polar oceans caused by the ORB effect, which reduced the freshwater flux export to the subpolar

21  Atlantic and resulted in a more saline North Atlantic. This study may help us quantitatively understand the role of

22  different external forcing factors in the Earth's climate evolution since the MH.

23  **Keywords**: mid-Holocene, Earth orbital parameters, Greenhouse gases, AMOC

24

25  ## 1. Introduction

26  The mid-Holocene (MH, 6000 years before the present) is a period of profound cultural transition worldwide,

27  particularly in the arid-semi-arid belt (~30°N) (Sandweiss et al., 1999; Moss et al., 2007; Roberts et al., 2011; Warden

28  et al., 2017). The MH climate, which belongs to the Holocene climatic optimum (Rossignol-Strick, 1999; Chen et al.,

29  2003; Zhang et al., 2020), is significant different from the subsequent period. Many studies have shown that the

30  development of human civilization during this period was influenced by the climate, which was closely related to

31  external factors such as the Earth's orbital parameters (ORB), greenhouse gases (GHG) and solar constants (Jin, 2002;

32  Wanner et al., 2008; Warden et al., 2017). Therefore, it is of great interest to study the MH climate, for a better

33  understanding of the influence of external forcing factors on human civilization.

34      As the key benchmark period of the Paleoclimate Modeling Intercomparison Project (PMIP) program, starting

35  with the earliest PMIP program (Joussaume and Taylor, 1995; Kageyama et al., 2018), the MH experiment was

36  designed to examine the climate response to a change in the seasonal and latitudinal distribution of incoming solar

37  radiation caused by known changes in Earth orbital forcing. As the program evolved, the GHG concentrations used in

38  the MH experiments are closer to the true values (Monnin et al., 2001, 2004). However, most studies focused on the

39  general climate differences between the MH and pre-industrial (PI) periods; the individual effects of the ORB and

40  GHG on the climate are not isolated. Some studies examined the role of GHG by comparing the PMIP programs.

41  Otto-Bliesner et al. (2017) found that the change in the experimental protocol between PMIP4 and PMIP3, with a

42  reduction in $CO_2$ concentration from 280 to 264.4 ppm, would reduce GHG forcing by about 0.3 W/m$^{-2}$. This change

43  can produce an estimated global mean cooling in surface air temperature (SAT) of about -0.28℃ based on the climate

44  sensitivity of each model in PMIP4 (Brierley et al., 2020). Note that the differences in the MH experiments between

45  PMIP4 and PMIP3 include only the GHG effect: the GHG contribution to temperature change is not negligible

46  although it is small. Quantifying the effects of ORB and GHG on the difference between the MH and PI is much

47  needed. Explaining this issue clearly has important implications for a deeper understanding of the role played by

48  external forcing factors in the past climate.

49      The Atlantic meridional overturning circulation (AMOC) is considered an important heat transmitter of the

50  Earth's climate system, which affects global climate on multiple timescales (Rahmstorf, 2006). Paleoclimate studies

51  showed that the weakening or stopping of the AMOC will lead to a large-scale drastic cooling in the Northern

52  Hemisphere (NH)  (Brown and Galbraith, 2016; Yan and Liu, 2019). Therefore, studying past AMOC changes will

53  help us understand the nature of climate change in the past and better predict future climate. In the previous MH

54  simulations of the PMIP, the AMOC is generally stronger than that of the PI (Găinuşă-Bogdan et al., 2020), but these

55  simulation results may be slightly different due to model or resolution differences (Shi and Lohmann, 2016; Shi et al.,

56  2022). Recent studied suggested that the difference of the AMOC between the MH and PI periods is not significant

57  (Brierley et al., 2020). By comparing the strength of the AMOC during the interglacial period, it was found that the

58 variation range of the AMOC in the MH is within the internal variability range of all models; and the ORB does not

59 seem to have played a role (Jiang et al., 2023).

60       In this paper, we further study the mechanism of weak difference of the AMOC between the MH and PI periods.

61 The effects of different external forcing factors on the AMOC will be quantified. This paper is organized as follows.

62 An introduction to the fully coupled climate model is given in section 2, along with the experiments design. The

63 effects of ORB and GHG on the MH climate, the AMOC, and Hadley cell are shown in section 3. The changes of

64 North Atlantic Ocean buoyancy are described in section 4. Summary and discussion are given in section 5.

65

66 **2. Model and experiments**

67       The National Centre for Atmospheric Research's Community Earth System Model version 1.0 (CESM1.0) is

68 used in this study. The coupled model includes atmospheric, oceanic, sea-ice, and land model components. The

69 atmospheric model has 26 vertical levels and T31 horizontal resolution. The land model has the same horizontal

70 resolution as the atmospheric model. The ocean model has 60 vertical levels and gx3v7 horizontal resolution. The sea-

71 ice model has the same horizontal resolution as the ocean model. More details on these model components can be

72 found in a number of studies (Smith and Gregory, 2009; Hunke and Lipscomb, 2010; Lawrence et al., 2012; Park et

73 al., 2014).

74       To quantify the effects of ORB and GHG on climate differences between the MH and PI periods, we designed

75 three experiments following the PMIP4 protocol (Table 1). Experiment MH uses the ORB and GHG in the MH

76 period. Experiment MH_ORB uses the ORB in the MH period and the GHG in the PI period. Experiment PI uses the

77 ORB and GHG in the PI period. Specific values of the Earth orbital parameters are listed in Table 1 (Berger and

78 Loutre, 1991). The vernal equinox is set to noon on 21 March, and the solar constant is set to 1360.75 W/m$^2$ in all

79 three simulations. The GHG data comes from the ice-core records of the Antarctica and Greenland (Otto-Bliesner et

80 al., 2017). The three experiments are all integrated for 2000 years, with MH and MH_ORB starting from the PI

81 condition. In this paper, we use the monthly mean data of the last 500 years of each model simulation. The effect of

82 ORB is obtained by subtracting the Exp PI from the Exp MH_ORB, and the effect of GHG is obtained by subtracting

83 the Exp MH_ORB from the Exp MH. The combined effect of ORB and GHG is obtained by subtracting the Exp PI

84 from the Exp MH.

85

86

87    **Table 1. Forcing and boundary conditions. More details can be found in Otto-Bliesner et al. (2017)**

|  | Exp MH | Exp PI | Exp MH_ORB |
|---|---|---|---|
| Orbital parameters |  |  | Same as Exp MH |
| Eccentricity | 0.018682 | 0.016764 | 0.018682 |
| Obliquity (degrees) | 24.105 | 23.459 | 24.105 |
| Perihelion – 180 | 0.87 | 100.33 | 0.87 |
| Greenhouse gases |  |  | Same as Exp PI |
| $CO_2$ (ppm) | 264.4 | 284.3 | 284.3 |
| $CH_4$ (ppb) | 597 | 808.2 | 808.2 |
| $N_2O$ (ppb) | 262 | 273.0 | 273.0 |

88

89    ORB includes eccentricity, precession, and obliquity. In the past six millennia, the eccentricity and obliquity did

90    not change much. The main change came from precession, which is influenced by eccentricity and the longitude of

91    perihelion. As a result, perihelion is close to the NH autumn equinox in the MH period and close to the NH winter

92    solstice in the PI period. Therefore, with respect to Exp PI, the solar energy received at the top of the atmosphere

93    (TOA) in Exp MH changed seasonally and latitudinally, as shown in Fig. 1a. Compared to Exp PI, Exp MH had

94    higher NH summer radiation and lower winter radiation, and the difference during June–August (JJA) reached 30

95    $W/m^2$ in the high latitudes. Smaller precession led to more radiation received in the NH summer in the MH period.

96    Figure 1b shows the meridional variation of annual mean shortwave radiation at the TOA, which is greater than 4

97    $W/m^2$ poleward of 45°N(S), but negative and smaller than 1 $W/m^2$ between 45°S and 45°N. This situation is

98    associated with the larger obliquity in the MH (Otto-Bliesner et al., 2006; Williams et al., 2020). In addition, the

99    difference of GHG between the MH and PI periods can lead to an effective radiative forcing of 0.3 $W/m^2$ (Otto-

100   Bliesner et al., 2017).
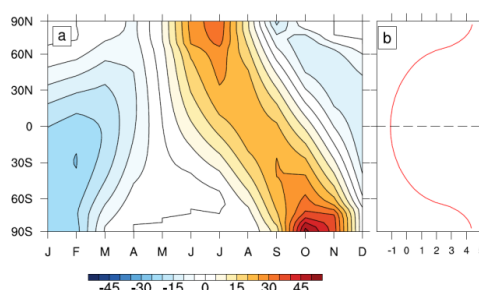
101

102   **Figure 1    (a) Latitude-month distribution of solar radiation change at the TOA in Exp MH, and (b) annual mean solar**

103   **radiation change, with respect to Exp PI. Units: $W/m^2$.**

104 **3. Results**

105 **3.1 Surface air temperature and precipitation**

106     Compared to Exp PI, Exp MH has warmer annual mean temperatures in the NH high latitudes and cooler

107 temperatures in the rest of the globe (Fig. 2a), while Exp MH_ORB has a warmer surface at mid–high latitudes in both

108 the NH and SH, with a greater range and magnitude than Exp MH (Fig. 2b). Figure 2b shows the direct response to the

109 meridional change of annual mean solar radiation. The lower GHG in the MH contributed to a lower global surface

110 temperature, which is clear in the mid–high latitudes (Fig. 2c). In the NH summer (June–August, or JJA), Exp MH

111 shows a general warming of more than 1℃ north of 30°N, which is more significant in Greenland and Euro-Asian

112 continent, and a cooling belt in northern India and central Africa (Fig. 2d), which is associated with increased rainfall

113 due to the enhanced monsoon (Fig. 3d). The magnitude and extent of warming due to the ORB effect are apparently

114 greater, with warming of up to 3℃ in central Asia (Fig. 2e). The GHG cooling is more pronounced over the Southern

115 Ocean (Fig. 2f). In the NH winter (December–February, or DJF), only the NH polar latitudes remain the warming.

116 There is strong cooling (up to 3℃) in the African and Euro-Asian continents (Fig. 2g). The patterns under the ORB

117 and GHG forcing are similar to their annual mean situations, except for the enhanced cooling in South Asia and

118 central Africa (Fig. 2h) and over the subpolar Atlantic (Fig. 2i). Most figures are featured with a polar amplification,

119 which may be related to the change of sea ice (Otto-Bliesner et al., 2017; Williams et al., 2020).
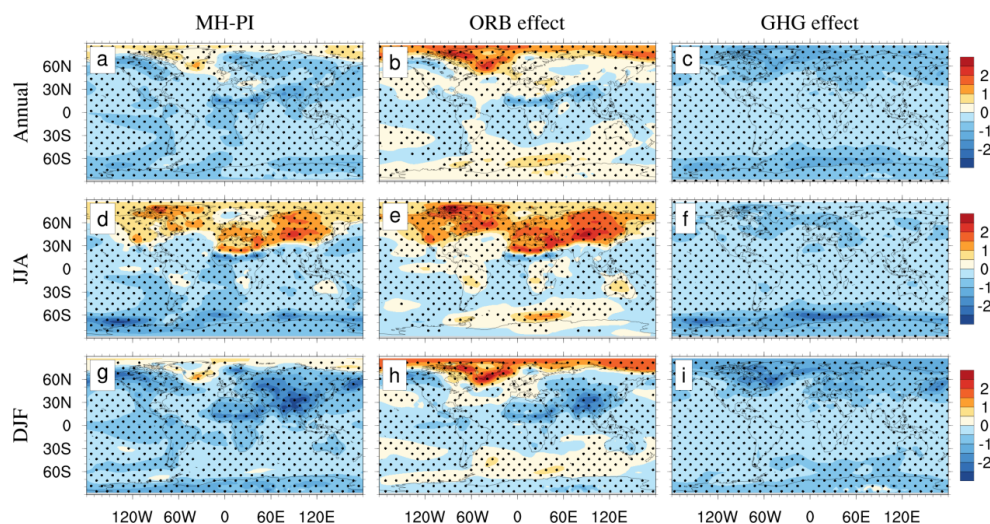
121 **Figure 2 (Left column) Changes in SAT in the Exp MH, with respect to the PI, and the contributions from (central**

122 **column) the ORB effect and (right column) the GHG effect. (a)–(c) are for annual mean; (d)–(f), for the NH JJA; and (g)–**

123 **(i), for the NH DJF. Stippling shows significance over the 90% level calculated by Student *t*-test. Units:℃.**

124

125    Differences in precipitation between the MH and PI simulations are shown in Fig. 3. Consistent with the

126    latitudinal and seasonal differences of insolation (Fig. 1), the largest difference in precipitation between the two

127    periods also occurs in the NH summer, with significantly more precipitation in northern India and in the equatorial

128    African monsoon region, and drier in the equatorial Atlantic and Pacific in Exp MH (Fig. 3d). The difference between

129    Exps MH and PI is mainly in the global tropics and is contributed predominantly by the ORB effect (Figs. 3e, h), as

130    the GHG effect is very weak (Figs. 3f, i).
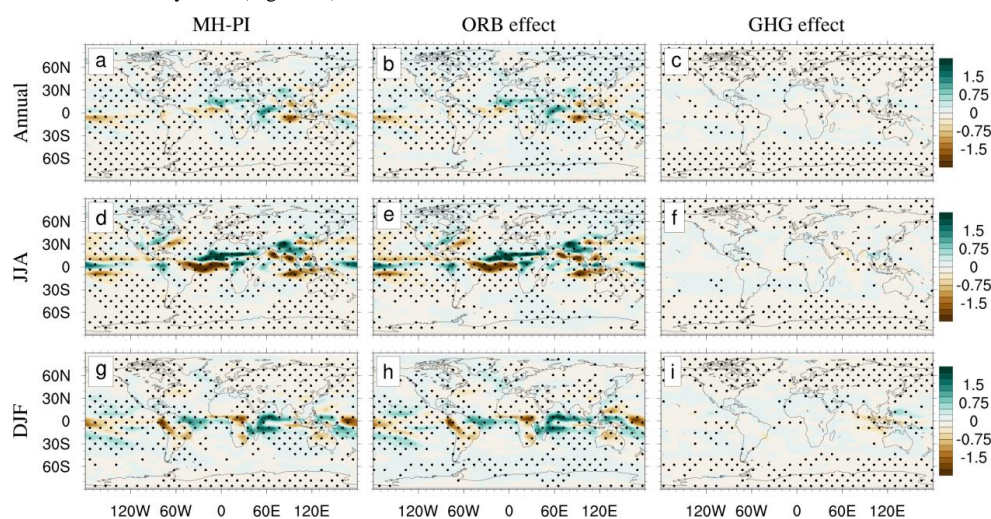
131

132    **Figure 3   Same as Fig. 2, but for precipitation change. Units: mm/day.**

133

134    Although the numerical values may be slightly different due to different models or resolutions, in general the

135    annual and seasonal climatology differences of temperature and precipitation between Exps MH and PI are in good

136    agreement in some recent studies (Williams et al., 2020; Zhang et al., 2021b). The ORB effect dominates the changes

137    in global surface temperature and precipitation. Exp MH has a warmer climate than Exp PI, particularly in the NH

138    high latitudes.

139

140    **3.2 Meridional atmospheric circulation**

141    The meridional atmospheric circulation, namely, the Hadley cell in Exp MH is about 10% weaker than that in

142    Exp PI (Fig. 4a), consistent with the weaker meridional atmospheric temperature gradient in Exp MH than in Exp PI.

143    The weaker Hadley cell in Exp MH is mainly due to the ORB effect (Figs. 4b, e, h). The GHG effect can be neglected

144    (Figs. 4c, f, i). The Hadley cell is weaker due to the strong warming of the high-latitude temperatures in the NH

145    summer (Fig. 4d). The strengthening of the Hadley cell in the NH winter (Fig. 4g) corresponds to an increasing

146    temperature gradient between the tropics and mid latitudes (Fig. 2g). The weaker Hadley cell also leads to a weaker

147    meridional atmospheric heat transport from low to high latitudes, which will be discussed in section 3.4.
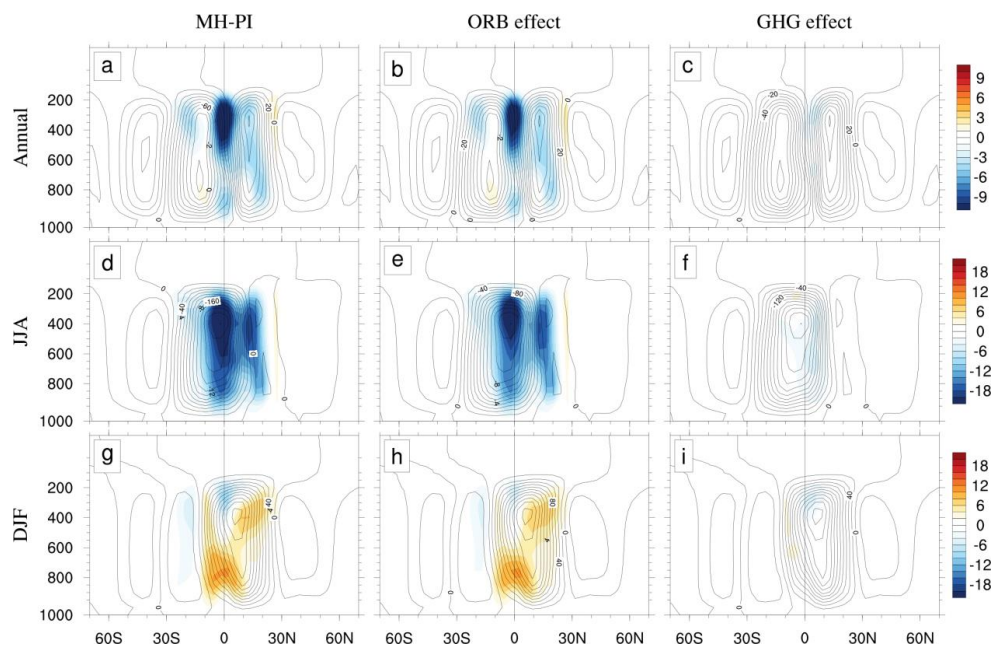
148
149    **Figure 4   Same as Fig. 2, but for the mean Hadley cell in Exp PI (contour) and its changes (shading) in Exp MH. Units: 10⁹**

150    **kg/s.**

151

152    **3.3 AMOC**

153         The AMOC strength, defined as the maximum streamfunction between 0–2000 m and 20°–70°N in the North

154    Atlantic, are 19.4 and 18.3 Sv in Exps MH and PI, respectively. The depth of the maximum AMOC in all experiments

155    occurs near 1000 m. The AMOC patterns in Exps MH and PI are similar (Figs. 4a, c), which suggests that the

156    combined effect of the ORB and GHG on the AMOC is small (Fig. 4d). However, individual effects of the ORB and

157    GHG are not negligible (Figs. 4e, f). In fact, the ORB effect leads to 6% stronger AMOC in Exp MH than in Exp PI

158    (Fig. 5e). The deep overturning is significantly enhanced south of 45°N, but slightly weakened north of 45°N.

159    However, at the same time the GHG effect leads to a slight decline in AMOC strength in Exp MH, especially above

160    1500 m south of 45°N (Fig. 5f). The ORB and GHG have the opposite effects on the AMOC, which make the AMOC

161    in Exp MH roughly the same as that in Exp PI. This is different from most previous findings (Otto-Bliesner et al.,

162  2006; Shi and Lohmann, 2016). In section 4, we will explain the mechanism of weak enhancement of the AMOC by

163  presenting the changes in the North Atlantic.
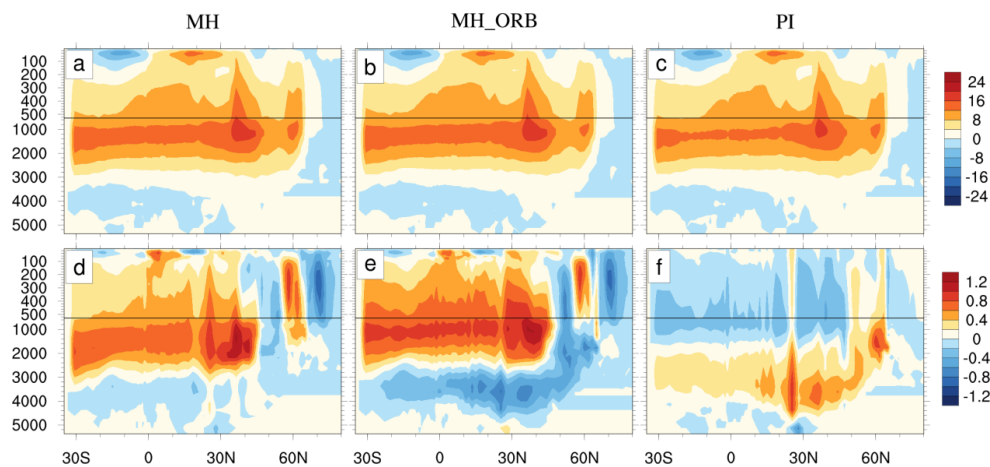
165  **Figure 5  Patterns of mean AMOC in (a) Exp MH, (b) Exp MH_ORB, and (c) Exp PI; and (d) the AMOC change in Exp**

166  **MH, with respect to Exp PI. (d) and (e) show the AMOC changes due to the ORB effect and GHG effect, respectively. The**

167  **AMOC index is defined as the maximum streamfunction in the range of 0–2000 m of 20°–70°N in the North Atlantic. Units:**

168  **Sv (1 Sv=10⁶ m³/s).**

169

170  **3.4 Meridional heat transport**

171      Meridional heat transport (MHT) plays an important role in maintaining energy balance of the Earth climate

172  system. Figure 6a shows the annual MHTs in different experiments, which are nearly identical. The climate

173  differences between Exps MH and PI hardly change the integrated heat transport in both the atmosphere and ocean.

174  Consistent with previous studies (Trenberth and Caron, 2001), the annual mean MHT shows an antisymmetric

175  structure about the equator, with the peak value of about 5.5 PW (1 PW=$10^{15}$W) at 40°N/S. Compared with ocean

176  heat transport (OHT), the atmosphere heat transport (AHT) dominates at most latitudes, which is also consistent with

177  most studies (Held, 2001; Wunsch, 2005; Czaja and Marshall, 2006).

178      However, the MHT changes caused by the ORB and GHG effects appear to be nonnegligible. The ORB causes

179  an increase in OHT in the NH, with the maximum change of about 0.10 PW near the equator, roughly 10% of the

180  mean OHT there. This is due to the enhanced AMOC and is the main cause of temperature increase in the NH high

181  latitudes (Fig. 2b). The northward AHT is reduced, with the maximum change of about 0.10 PW. This is due to the

182  weakend Hadley cell. The AHT change compensates the OHT change very well in the deep tropics, while the former

183  overcompensats the latter in the NH off-equatorial regions (Fig. 6b). The GHG effect on the MHT is very weak, with

184    the maximum MHT change of no more than 0.04 PW near 5°N, which is just one third of the ORB-induced MHT

185    change (Fig. 6c).
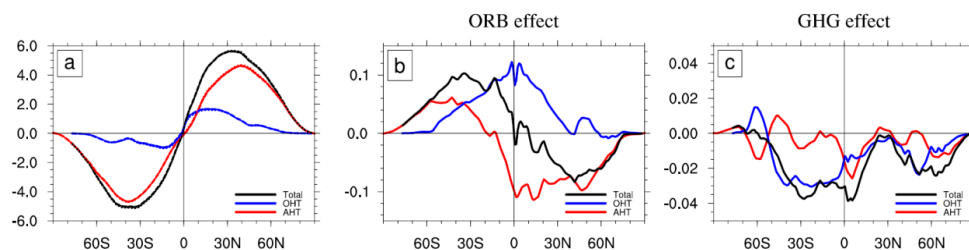
186

187    **Figure 6  (a) Annual mean meridional heat transport (MHT). Black, red, and blue for the total MHT, AHT, and OHT,**

188    **respectively. Solid, dashed, and dotted for Exps MH, MH_ORB, and PI, respectively. (b) and (c) show changes in the total**

189    **MHT, AHT, and OHT due to ORB and GHG effects, respectively. Units: PW (1 PW = $10^{15}$ W).**

190

191    **4.  Changes in the North Atlantic Ocean**

192    **4.1 Changes in sea-surface temperature, salinity, and density**

193        The strength of the AMOC is largely determined by the North Atlantic deep-water formation, which is in turn

194    determined by upper-ocean density. Figure 7 shows the differences of sea-surface temperature (SST), salinity (SSS),

195    and density (SSD) in the North Atlantic between Exps MH and PI. The SST difference is characterized by a warming

196    up to 1.6℃ in the subpolar Atlantic and a cooling of about 1℃ near the Nordic Seas and Gulf Stream extension region

197    (Fig. 7a). The surface ocean warming in the North Atlantic is due to the ORB effect (Fig. 7b), which causes a strong

198    and extensive warming in the North Atlantic, with the maximum warming in the subpolar Atlantic. The GHG effect

199    causes a general cooling in the North Atlantic (Fig. 7c), offsetting partially the ORB-induced warming, leaving a

200    cooling in the Nordic Seas and Gulf Stream extension (Fig. 7a).

201        The patterns of SSS difference between Exps MH and PI are similar to those of SST difference. In general, the

202    North Atlantic is more saline in Exp MH than in Exp PI (Fig. 7d), mainly due to stronger evaporation over

203    precipitation in Exp MH than in Exp PI (Fig. 9d), which is in turn due to the warmer SST forced by the ORB effect

204    (Fig. 7e). The polar oceans are fresher in Exp MH than in Exp PI (Figs. 7d, e), mainly, due to more freshwater flux

205    coming from the sea ice in Exp MH (Figs. 9a, b), consistent with the warmer climate in the MH due to the ORB effect.

206    The SSS difference caused by the GHG effect is roughly opposite to that caused by the ORB effect, but with much

207    weaker magnitude (Fig. 7f), because the cooling effect of the GHG makes less evaporation in the subtropical to

208    subpolar Atlantic and more sea ice in the polar oceans (Fig. 9c).

209    The patterns of SSD difference (Figs. 7g–i) resemble those of both SSS and SST differences, while its polarity is

210    determined by SSS difference. The higher SSD in the North Atlantic is favorable to stronger deep-water formation and

211    thus a stronger AMOC in Exp MH. Forced by the ORB effect, the North Atlantic surface ocean can be 0.5 kg/m$^3$

212    denser in Exp MH than in Exp PI (Fig. 7h), which could have resulted in 1.2-Sv stronger AMOC in Exp MH than in

213    Exp PI (Fig. 5e). However, the GHG effect, although weak, has an opposite effect on SSD and thus the AMOC (Fig.

214    7i), and eventually mitigates the ocean change in Exp MH.
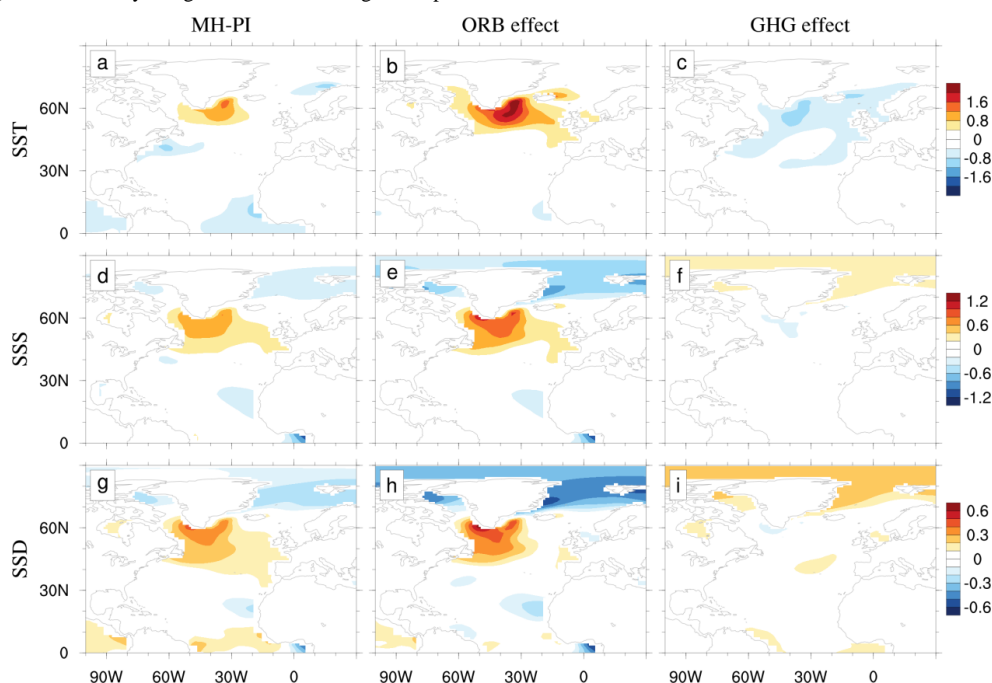
215

216    **Figure 7  Changes in (a)–(c) sea-surface temperature (SST), (d)–(f) sea-surface salinity (SSS), and (g)–(i) sea-surface density**

217    **(SSD) of the North Atlantic in Exp MH, with respect to the Exp PI. (a), (d), and (g) are for the total changes; (b), (e), and**

218    **(h), for the changes due to ORB effect. (c), (f), and (i) are for changes due to GHG effect. Units are ℃ for SST, psu for SSS,**

219    **and kg/m$^3$ for SSD.**

220

221    **4.2 Change in surface freshwater flux**

222    Sea-surface freshwater flux includes both sea-ice formation (melting) and net evaporation (i.e., evaporation

223    minus precipitation, or EMP). Figure 8 shows the change of annual mean sea-ice thickness in the Arctic. The Arctic

224    sea-ice thickness in Exp MH is about 1.0 m thinner than that in Exp PI (Fig. 8a). The largest sea-ice difference, which

225    is about 3.0 m thinner in Exp MH, occurs in the Baffin Bay. Forced by the ORB effect only, the Arctic sea ice would

226    be more than 1.5 m thinner (Fig. 8b), consistent with the stronger insolation and the warming in the NH high latitudes

227   (Figs. 1, 2e). The GHG effect leads to a slight increase of sea ice in the Arctic (Fig. 8c) in Exp MH, which is less than

228   0.5 m in thickness. Changes in Arctic sea ice thickness can affect sea-ice transport to the subpolar Atlantic. The loss of

229   sea ice in the central Arctic Ocean can reduce its export through the Fram Strait, which can lead to an increase in

230   salinity in the associated sub-polar regions (Shi and Lohmann, 2016), as shown in Figs. 7d and e.

231
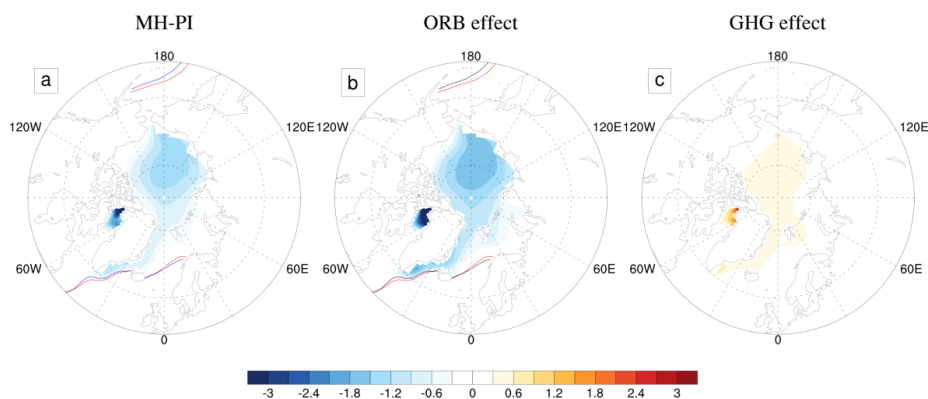
**Figure 8   Changes in the Arctic mean sea-ice thickness in Exp MH, with respect to Exp PI. Positive (negative) value represents sea-ice formation (melting). (a) for total change; (b) and (c) for changes due to ORB and GHG effects, respectively. Solid blue, black, and red curves show the sea-ice margin in Exps MH, MH_ORB and PI, respectively. The sea-ice margin is defined by the 15% sea-ice fraction. Units: m.**

236

237        The sea-ice margin in the North Atlantic in Exp MH is slightly more northward compared to that in Exp PI (solid

238   blue curve, Fig. 8a). The curves in Fig. 8 show sea-ice margin in different experiments. The northward displacement

239   of sea-ice margin and the decrease in ice volume in the Arctic favor the decrease in freshwater flux in the North

240   Atlantic, helping a more saline North Atlantic, which contributes about 0.9 psu 10yr$^{-1}$ to the SSS tendency between

241   40° and 60°N (Fig. 9a). The EMP flux is small, and the upper ocean is refreshed at a steady rate of about 0.09 psu

242   10yr$^{-1}$ in the North Atlantic (Fig. 9d). Overall, for the North Atlantic the change of sea ice plays a dominant role; and

243   its contribution to SSS tendency is about 10 times that of EMP.
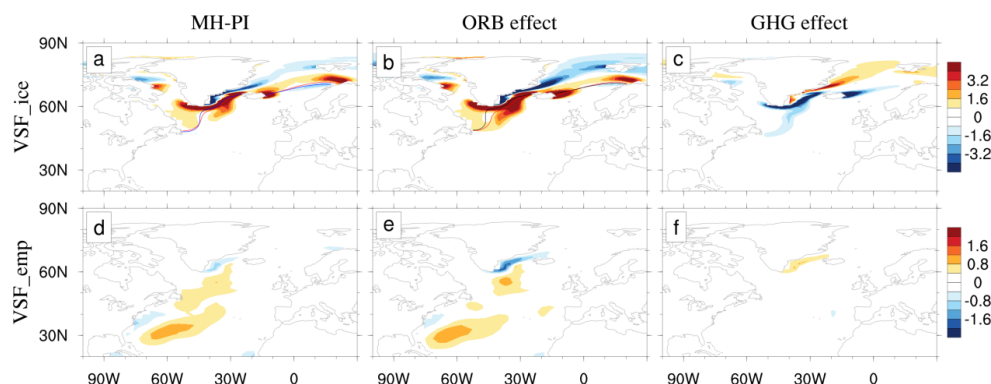
**Figure 9  Changes in (a)–(c) are virtual salt flux (VSF) due to sea ice, and in (d)–(f), VSF due to EMP in Exp MH, with respect to Exp PI. Positive (negative) value represents sea-ice formation (melting) or evaporation larger (smaller) than precipitation. (a) and (d) for total changes; (b) and (e) for changes due to ORB effect; (c) and (f) for GHG effect. The sea-ice margin in (a)–(b) are the same as those in Fig. 8. Units: psu 10 yr$^{-1}$.**

The sea-ice margin in Exp MH is controlled by the ORB effect. In individual forcing experiment, the sea-ice margin forced by the ORB effect is almost the same as that in Exp MH (solid black curve, Fig. 9b). The contributions of ORB and GHG effects to changes in virtual salt flux (VSF) due to sea ice are 1.3 and -0.4 psu 10yr$^{-1}$, respectively (Figs. 9b, c); and those due to the EMP flux are 0.06 and 0.03 psu 10yr$^{-1}$, respectively (Figs. 9e, f). The sea-ice change caused by the ORB effect plays an important role in the enhancement of the AMOC in Exp MH.

In general, the modelling results suggest that the stronger AMOC in Exp MH is resulted from more saline North Atlantic, which is contributed mainly by smaller freshwater flux coming from the Arctic. The contribution of EMP to salinity change is small, which is only one-tenth of sea-ice contribution. ORB and GHG consistently play opposite roles in the deep-water formation of the subpolar Atlantic. Their combined effect results in little change in the AMOC in Exp MH, with only about 0.8 Sv enhancement.

## 5.  Summary and discussion

In this study, three experiments using the CESM1.0 were conducted to quantify the contributions of ORB and GHG effects to the MH climate. More attention was paid to the AMOC; and the mechanism to the insignificant difference of the AMOC between the MH and PI periods was explored. This study is the first attempt to separate the ORB and GHG effects on the MH climate. Simulations show that the NH climate exhibits much greater regional and seasonal variability due to the seasonal enhancement of insolation caused by changes in ORB; and these contrasting

267  seasonal responses lead to little change in annual mean climate (Fig. 2b). Lower GHG in Exp MH has a global cooling

268  effect, with greater temperature decreases at higher latitudes associated with feedbacks from sea ice and snow cover

269  (Fig. 2c). The combined effect of these two forcing factors leads to a weak warming at the NH high latitudes and

270  cooling elsewhere (Fig. 2a), similar to the temperature changes in the PMIP4 ensemble (Brierley et al., 2020)

271      Weakening meridional atmospheric temperature gradient in Exp MH leads to the Hadley cell being weakened by

272  about 10% in the NH (Fig. 4a). At the same time, due to the change of sea-surface buoyancy in the North Atlantic, the

273  AMOC is slightly enhanced by about 4% (Fig. 5a). As far as the changes in MHT magnitude in the NH are concerned,

274  the effect of ORB is about five times that of GHG (Figs. 6b, c). Our experiments also show that the change in AMOC

275  is mostly determined by the freshwater flux change in the North Atlantic, which is in turn closely related to the Arctic

276  sea-ice change related to the ORB effect. GHG has the opposite effect to ORB, which mitigates the enhancement of

277  the AMOC (Figs. 9b, c).

278      The conclusions drawn in this paper may be model-dependent. Shi and Lohmann, (2016) simulated a stronger

279  MH AMOC in the high-resolution version of the ECHAM, with a maximum change of more than 2 Sv. Most of the

280  models in the CMIP5 ensemble reveal a positive AMOC change in the MH period. Some previous studies (Ganopolski

281  et al., 1998; Otto-Bliesner et al., 2006) showed that the AMOC in the MH is weaker than that of the PI period. The

282  main reason for the inconsistency is that the simulated ocean salinity in the North Atlantic is different. In addition to

283  the model itself, whether the experimental setting includes the GHG is also an important factor. Our results on the

284  AMOC in the MH are similar to those of  (Jiang et al., 2023), but our focus is to find the mutual offsetting effect

285  between external forcing factors. The experiments we conducted are time-slice experiments. And it is necessary to

286  study whether the offsetting effects of the ORB and GHG exists in transient experiments.

287      Our experiments only consider the ORB and GHG effects; and the simulated cooler annual mean temperature

288  over most areas of the NH differs from the warming record revealed by proxy data (Wanner et al., 2008; Liu et al.,

289  2014), but is similar to the conclusions from the PMIP4 ensemble simulations. It is unclear whether these differences

290  originate from the model, the data record, or a combination of both. Some proxy data suggested that the climate of

291  North Africa was wetter in the MH period, which was known as the Green Sahara. (Jiang et al., 2012) analyzeed six

292  sets of PMIP2 coupled models' results, and found that the dynamic vegetation has little impact on regional climate.

293  Braconnot et al. (2021) and Zhang et al. (2021a) studied the effect of dust reduction on climate due to the greening of

294  the Sahara desert, using the CESM and IPSL models, respectively, showing global mean surface temperature

295  increased by about 0.1℃. Although there are other forcing factors in the MH period, such as vegetation, dust, and

296    topography, overall our simulations are representative of the most important forcing factors and provide quantified

297    estimates of the contributions of ORB and GHG effects to the MH climate.

298

299    **Acknowledgements.** This work is supported by the National Natural Science Foundation of China (No. 42230403).

300    The experiments were performed on the supercomputers at the Chinese National Supercomputer Centre in Tianjin

301    (Tian-He No.1).

302

303 **References**

304 Berger, A. and Loutre, M. F.: Insolation values for the climate of the last 10 million years, Quaternary Sci. Rev., 10,

305     297-317, https://doi.org/10.1016/0277-3791(91)90033-Q, 1991.

306 Braconnot, P., Albani, S., Balkanski, Y., Cozic, A., Kageyama, M., Sima, A., Marti, O., and Peterschmitt, J. Y.:

307     Impact of dust in PMIP-CMIP6 mid-Holocene simulations with the IPSL model, Clim. Past, 17, 1091-1117,

308     http://doi.org/10.5194/cp-17-1091-2021, 2021.

309 Brierley, C. M., Zhao, A., Harrison, S. P., Braconnot, P., Williams, C. J. R., Thornalley, D. J. R., Shi, X., Peterschmitt,

310     J.-Y., Ohgaito, R., Kaufman, D. S., Kageyama, M., Hargreaves, J. C., Erb, M. P., Emile-Geay, J., D'Agostino, R.,

311     Chandan, D., Carré, M., Bartlein, P. J., Zheng, W., Zhang, Z., Zhang, Q., Yang, H., Volodin, E. M., Tomas, R.

312     A., Routson, C., Peltier, W. R., Otto-Bliesner, B., Morozova, P. A., McKay, N. P., Lohmann, G., Legrande, A.

313     N., Guo, C., Cao, J., Brady, E., Annan, J. D., and Abe-Ouchi, A.: Large-scale features and evaluation of the

314     PMIP4-CMIP6 <i>midHolocene</i> simulations, Clim. Past, 16, 1847-1872,

315     https://doi.org/10.5194/cp-16-1847-2020, 2020.

316 Brown, N. and Galbraith, E. D.: Hosed vs. unhosed: interruptions of the Atlantic Meridional Overturning Circulation

317     in a global coupled model, with and without freshwater forcing, Clim. Past, 12, 1663-1679,

318     https://doi.org/10.5194/cp-12-1663-2016, 2016.

319 Chen, C.-T. A., Lan, H.-C., Lou, J.-Y., and Chen, Y.-C.: The Dry Holocene Megathermal in Inner Mongolia,

320     Palaeogeogr. Palaeoclimatol. Palaeoecol., 193, 181-200, https://doi.org/10.1016/s0031-0182(03)00225-6, 2003.

321 Czaja, A. and Marshall, J.: The Partitioning of Poleward Heat Transport between the Atmosphere and Ocean, Global

322     Planet. Change., 63, 1498-1511, https://doi.org/10.1175/jas3695.1, 2006.

323 Găinuşă-Bogdan, A., Swingedouw, D., Yiou, P., Cattiaux, J., Codron, F., and Michel, S.: AMOC and summer sea ice

324     as key drivers of the spread in mid-holocene winter temperature patterns over Europe in PMIP3 models, Global

325     Planet. Change., 184, https://doi.org/10.1016/j.gloplacha.2019.103055, 2020.

326 Ganopolski, A., Kubatzki, C., Claussen, M., Brovkin, V., and Petoukhov, V.: The Influence of Vegetation-

327     Atmosphere-Ocean Interaction on Climate During the Mid-Holocene, Science, 280, 1916-1919,

328     https://doi.org/10.1126/science.280.5371.1916, 1998.

329 Held, I. M.: The Partitioning of the Poleward Energy Transport between the Tropical Ocean and Atmosphere, J.

330     Atmos. Sci, 58, 943-948, https://doi.org/10.1175/1520-0469(2001)058<0943:Tpotpe>2.0.Co;2, 2001.

331   Hunke, E. C. and Lipscomb, W. H.: CICE: The Los Alamos Sea Ice Model documentation and software user's

332     manual, version 4.1. Doc. LACC-06-012, 76, CICE_documentation_and_software_user's_manual.pdf

333     (colorado.edu), 2010.

334   Jiang, D., Lang, X., Tian, Z., and Wang, T.: Considerable Model–Data Mismatch in Temperature over China during

335     the Mid-Holocene: Results of PMIP Simulations, J. Climate, 25, 4135-4153, https://doi.org/10.1175/jcli-d-11-

336     00231.1, 2012.

337   Jiang, Z., Brierley, C., Thornalley, D., and Sax, S.: No changes in overall AMOC strength in interglacial PMIP4 time

338     slices, Clim. Past, 19, 107-121, https://doi.org/10.5194/cp-19-107-2023, 2023.

339   Jin, G.: Mid-Holocene climate change in North China, and the effect on cultural development, Chinese Sci. Bull, 47,

340     https://doi.org/10.1360/02tb9095, 2002.

341   Joussaume, S. and Taylor, K.: Status of the paleoclimate modeling intercomparison project (PMIP), World

342     Meteorological Organization-Publications-WMO TD, 425-430, 1995.

343   Kageyama, M., Braconnot, P., Harrison, S. P., Haywood, A. M., Jungclaus, J. H., Otto-Bliesner, B. L., Peterschmitt,

344     J.-Y., Abe-Ouchi, A., Albani, S., Bartlein, P. J., Brierley, C., Crucifix, M., Dolan, A., Fernandez-Donado, L.,

345     Fischer, H., Hopcroft, P. O., Ivanovic, R. F., Lambert, F., Lunt, D. J., Mahowald, N. M., Peltier, W. R., Phipps, S.

346     J., Roche, D. M., Schmidt, G. A., Tarasov, L., Valdes, P. J., Zhang, Q., and Zhou, T.: The PMIP4 contribution to

347     CMIP6 – Part 1: Overview and over-arching analysis plan, Geosci. Model. Dev., 11, 1033-1057,

348     https://doi.org/10.5194/gmd-11-1033-2018, 2018.

349   Lawrence, D. M., Oleson, K. W., Flanner, M. G., Fletcher, C. G., Lawrence, P. J., Levis, S., Swenson, S. C., and

350     Bonan, G. B.: The CCSM4 Land Simulation, 1850–2005: Assessment of Surface Climate and New Capabilities,

351     J. Climate, 25, 2240-2260, https://doi.org/10.1175/jcli-d-11-00103.1, 2012.

352   Liu, Z., Zhu, J., Rosenthal, Y., Zhang, X., Otto-Bliesner, B. L., Timmermann, A., Smith, R. S., Lohmann, G., Zheng,

353     W., and Elison Timm, O.: The Holocene temperature conundrum, P. Natl. Acad. Sci. USA, 111, E3501-3505,

354     https://doi.org/10.1073/pnas.1407229111, 2014.

355   Monnin, E., Indermu¨hle, A., Da¨llenbach, A., Flu¨ckiger, J., Stauffer, B., Stocker, T. F., Raynaud, D., and Barnola,

356     J.-M.: Atmospheric CO2 Concentrations over the Last Glacial Termination, Science, 291, 112-114,

357     https://doi.org/10.1126/science.291.5501.112, 2001.

358   Monnin, E., Steig, E. J., Siegenthaler, U., Kawamura, K., Schwander, J., Stauffer, B., Stocker, T. F., Morse, D. L.,

359     Barnola, J.-M., Bellier, B., Raynaud, D., and Fischer, H.: Evidence for substantial accumulation rate variability in

360    Antarctica during the Holocene, through synchronization of CO 2 in the Taylor Dome, Dome C and DML ice

361    cores, Earth Planet. Sc. Lett., 224, 45-54, https://doi.org/10.1016/j.epsl.2004.05.007, 2004.

362    Moss, M. L., Peteet, D. M., and Whitlock, C.: Mid-Holocene culture and climate on the Northwest Coast of North

363    America, in: Climate Change and Cultural Dynamics, 491-529, https://doi.org/10.1016/b978-012088390-

364    5.50019-4, 2007.

365    Otto-Bliesner, B. L., Brady, E. C., Clauzet, G., Tomas, R., Levis, S., and Kothavala, Z.: Last Glacial Maximum and

366    Holocene Climate in CCSM3, J. Climate, 19, 2526-2544, https://doi.org/10.1175/jcli3748.1, 2006.

367    Otto-Bliesner, B. L., Braconnot, P., Harrison, S. P., Lunt, D. J., Abe-Ouchi, A., Albani, S., Bartlein, P. J., Capron, E.,

368    Carlson, A. E., Dutton, A., Fischer, H., Goelzer, H., Govin, A., Haywood, A., Joos, F., LeGrande, A. N.,

369    Lipscomb, W. H., Lohmann, G., Mahowald, N., Nehrbass-Ahles, C., Pausata, F. S. R., Peterschmitt, J.-Y.,

370    Phipps, S. J., Renssen, H., and Zhang, Q.: The PMIP4 contribution to CMIP6 – Part 2: Two interglacials,

371    scientific objective and experimental design for Holocene and Last Interglacial simulations, Geosci. Model. Dev.,

372    10, 3979-4003, https://doi.org/10.5194/gmd-10-3979-2017, 2017.

373    Park, S., Bretherton, C. S., and Rasch, P. J.: Integrating Cloud Processes in the Community Atmosphere Model,

374    Version 5, J. Climate, 27, 6821-6856, https://doi.org/10.1175/jcli-d-14-00087.1, 2014.

375    Rahmstorf, S.: Thermohaline Ocean Circulation, in: Encyclopedia of Quaternary Sciences, edited by: Elias, S. A.,

376    Elsevier, Amsterdam, 1–10, 2006.

377    Roberts, N., Eastwood, W. J., Kuzucuoğlu, C., Fiorentino, G., and Caracuta, V.: Climatic, vegetation and cultural

378    change in the eastern Mediterranean during the mid-Holocene environmental transition, The Holocene, 21, 147-

379    162, https://doi.org/10.1177/0959683610386819, 2011.

380    Rossignol-Strick, M.: The Holocene climatic optimum and pollen records of sapropel 1 in the eastern Mediterranean,

381    9000–6000BP, Quaternary Sci. Rev., 18, 515-530, https://doi.org/10.1016/S0277-3791(98)00093-6, 1999.

382    Sandweiss, D. H., Maasch, K. A., and Anderson, D. G.: Transitions in the Mid-Holocene, Science, 283, 499-500,

383    https://doi.org/10.1126/science.283.5401.499, 1999.

384    Shi, X. and Lohmann, G.: Simulated response of the mid-Holocene Atlantic meridional overturning circulation in

385    ECHAM6-FESOM/MPIOM, J. Geophys. Res.-Oceans, 121, 6444-6469, https://doi.org/10.1002/2015jc011584,

386    2016.

387    Shi, X., Werner, M., Wang, Q., Yang, H., and Lohmann, G.: Simulated Mid-Holocene and Last Interglacial Climate

388    Using Two Generations of AWI-ESM, J. Climate, 35, 4211-4231, https://doi.org/10.1175/jcli-d-22-0354.1, 2022.

389  Smith, R. S. and Gregory, J. M.: A study of the sensitivity of ocean overturning circulation and climate to freshwater

390      input in different regions of the North Atlantic, Geophys. Res. Lett., 36, https://doi.org/10.1029/2009gl038607,

391      2009.

392  Trenberth, K. E. and Caron, J. M.: Estimates of Meridional Atmosphere and Ocean Heat Transports, J. Climate, 14,

393      3433-3443, https://doi.org/10.1175/1520-0442(2001)014<3433:Eomaao>2.0.Co;2, 2001.

394  Wanner, H., Beer, J., Bütikofer, J., Crowley, T. J., Cubasch, U., Flückiger, J., Goosse, H., Grosjean, M., Joos, F.,

395      Kaplan, J. O., Küttel, M., Müller, S. A., Prentice, I. C., Solomina, O., Stocker, T. F., Tarasov, P., Wagner, M.,

396      and Widmann, M.: Mid- to Late Holocene climate change: an overview, Quaternary Sci. Rev., 27, 1791-1828,

397      https://doi.org/10.1016/j.quascirev.2008.06.013, 2008.

398  Warden, L., Moros, M., Neumann, T., Shennan, S., Timpson, A., Manning, K., Sollai, M., Wacker, L., Perner, K.,

399      Häusler, K., Leipe, T., Zillén, L., Kotilainen, A., Jansen, E., Schneider, R. R., Oeberst, R., Arz, H., and Sinninghe

400      Damsté, J. S.: Climate induced human demographic and cultural change in northern Europe during the mid-

401      Holocene, Sci. Rep-UK, 7, https://doi.org/10.1038/s41598-017-14353-5, 2017.

402  Williams, C. J. R., Guarino, M.-V., Capron, E., Malmierca-Vallet, I., Singarayer, J. S., Sime, L. C., Lunt, D. J., and

403      Valdes, P. J.: CMIP6/PMIP4 simulations of the mid-Holocene and Last Interglacial using HadGEM3:

404      comparison to the pre-industrial era, previous model versions and proxy data, Clim. Past, 16, 1429-1450,

405      https://doi.org/10.5194/cp-16-1429-2020, 2020.

406  Wunsch, C.: The Total Meridional Heat Flux and Its Oceanic and Atmospheric Partition, J. Climate, 18, 4374-4380,

407      https://doi.org/10.1175/jcli3539.1, 2005.

408  Yan, M. and Liu, J.: Physical processes of cooling and mega-drought during the 4.2 ka BP event: results from

409      TraCE-21ka simulations, Clim. Past, 15, 265-277, https://doi.org/10.5194/cp-15-265-2019, 2019.

410  Zhang, J., Kong, X., Zhao, K., Wang, Y., Liu, S., Wang, Z., Liu, J., Cheng, H., and Edwards, R. L.: Centennial-scale

411      climatic changes in Central China during the Holocene climatic optimum, Palaeogeogr. Palaeoclimatol.

412      Palaeoecol., 558, https://doi.org/10.1016/j.palaeo.2020.109950, 2020.

413  Zhang, M., Liu, Y., Zhang, J., and Wen, Q.: AMOC and Climate Responses to Dust Reduction and Greening of

414      Sahara during the Mid-Holocene, J. Climate, 1-59, https://doi.org/10.1175/jcli-d-20-0628.1, 2021a.

415  Zhang, Q., Berntell, E., Axelsson, J., Chen, J., Han, Z., de Nooijer, W., Lu, Z., Li, Q., Zhang, Q., Wyser, K., and

416      Yang, S.: Simulating the mid-Holocene, last interglacial and mid-Pliocene climate with EC-Earth3-LR, Geosci.

417      Model. Dev., 14, 1147-1169, https://doi.org/10.5194/gmd-14-1147-2021, 2021b.

418